CHEMISTRY

Rotary biomolecular motor-powered supramolecular colloidal motor

Jun Liu[1], Yingjie Wu[1]*, Yue Li[1], Ling Yang[2], Hao Wu[2]*, Qiang He[1,2]*

Cells orchestrate the motion and force of hundreds of protein motors to perform various mechanical tasks over multiple length scales. However, engineering active biomimetic materials from protein motors that consume energy to propel continuous motion of micrometer-sized assembling systems remains challenging. Here, we report rotary biomolecular motor-powered supramolecular (RBMS) colloidal motors that are hierarchically assembled from a purified chromatophore membrane containing F_OF_1-ATP synthase molecular motors, and an assembled polyelectrolyte microcapsule. The micro-sized RBMS motor with asymmetric distribution of F_OF_1-ATPases can autonomously move under light illumination and is collectively powered by hundreds of rotary biomolecular motors. The propulsive mechanism is that a transmembrane proton gradient generated by a photochemical reaction drives F_OF_1-ATPases to rotate for ATP biosynthesis, which creates a local chemical field for self-diffusiophoretic force. Such an active supramolecular architecture endowed with motility and biosynthesis offers a promising platform for intelligent colloidal motors resembling the propulsive units in swimming bacteria.

INTRODUCTION

Motility and biosynthesis are the two most indispensably inherent characteristics of living cells, manifesting substantial migration capability for growth, division, and development. In cells, different suborganelles, biomacromolecules, and molecular complexes actively interact with their environments by efficiently transforming and transferring materials, information, and energy in the coordinated form to produce self-adaptive motions capable of performing complex biological functions (*1*, *2*). Different kinds of active protein molecular machines play a key role in these basic biological processes through the consumption of adenosine triphosphate (ATP) (*3*). ATP is the main energy currency of the cell, which is produced by a rotary biomolecular motor protein, F_OF_1-ATP synthase [i.e., F_OF_1–adenosine triphosphatase (ATPase)] (*4*). The structure and work mechanism of F_OF_1-ATPase have been revealed experimentally and theoretically. In addition, the reconstitution of F_OF_1-ATPase on the cell-mimic polymer multilayer microcapsules has been performed, in which ATPase retains its biological activity (*5*). These F_OF_1-ATPase–functionalized polymer capsules can serve as an excellent model to study the synthesis and regulation of ATP on demand. On the other hand, the nanometer-sized motor proteins can generate a force at the level of piconewtons, and their collective action can be amplified up to kilonewtons so that complex biological functions such as muscle contraction and intracellular material transport can be realized (*6*). Given that the assembled F_OF_1-ATPase motor proteins on the polymer microcapsules should also generate a mechanical action or even directional motion of those microcapsules to better mimic the cellular function, however, it is still not reported yet.

Chemically powered colloidal motors capable of converting the stored chemical energy in the surrounding environments into mechanical motion (*7*–*9*) have received increasing attentions because of their promising applicability in many fields such as active target delivery (*10*–*15*), biosensing (*16*–*18*), and environment remediation (*19*–*21*). In particular, chemical self-assembly allows the incorporation of a variety of natural or synthetic polymers, enzymes, nanoparticles, and other biocompatible and degradable building blocks into the supramolecular assembles, which can endow the colloidal motors with cell-like structures and functions (*22*–*29*). Actually, supramolecular colloidal motors have been considered as one type of ideal candidates for cellular mimic models and also have a great potential for biomedical applications. However, the development of supramolecular colloidal motors is currently restricted by the inherent toxicity of the used chemical fuels, their unavailability within the living organisms, and the propulsion efficiency. Hence, engineering a motor protein-integrated supramolecular motor powered by biofuels widely available from the organism with controllable self-actuation remains a highly nontrivial challenge.

Here, we present a rotary biomolecular motor-powered supramolecular (RBMS) colloidal motor fabricated by a combination of the templated-assisted layer-by-layer self-assembly with a vesicle fusion method. The natural vesicles containing F_OF_1-ATPases and chromatophores are separated from a kind of photosynthetic bacteria and then assembled on the surface of polyelectrolyte multilayer microcapsules to produce RBMS motors with asymmetric distribution of F_OF_1-ATPases. Under light illumination, the embedded chromophores are activated to catalyze a photochemical reaction and thus generate a proton gradient across the natural membrane-functionalized polymer microcapsules. The proton gradient results in movement of protons through the transmembrane channel Fo of F_OF_1-ATPase on the as-prepared RBMS colloidal motors, which drives the clockwise rotation of F_OF_1-ATPase to synthesize ATP from the substrates, adenosine diphosphate (ADP) and inorganic phosphate (PO_4^{3-}; Pi). The rotation of F_OF_1-ATPases can collectively drive these as-assembled RBMS colloidal motors to autonomously swim, and their speed is dependent on the power of

[1]School of Medicine and Health, Harbin Institute of Technology, Yi Kuang Jie 2, Harbin 150080, China. [2]Wenzhou Institute, University of Chinese Academy of Sciences, 1 Jinlian Street, Wenzhou 325000, China.
*Corresponding author. Email: wuyingjie@hit.edu.cn (Y.W.); wuhao@ucas.ac.cn (H. W.); qianghe@hit.edu.cn (Q.H.)

light irradiation, substrate concentration, and the light wavelength used.

RESULTS

Preparation and characterization of RBMS colloidal motors

The RBMS colloidal motors were synthesized as schematically illustrated in Fig. 1. Briefly, the chromatophore vesicles containing F_OF_1-ATPase molecular motors were obtained from the cytoplasmic membrane of photosynthetic bacteria *Rhodobacter sphaeroides* by ultrasonication and ultracentrifuge at different centrifugal forces, following by sucrose concentration gradient centrifugation for purification. Second, five bilayers of negatively charged poly(styrenesulfonate) sodium (PSS) and positively charged poly(allylamine hydrochloride) (PAH) were alternately assembled on the surface of 3-μm silica particles via a layer-by-layer self-assembly technique according to a previous report (*30*). The $(PSS/PAH)_5$ microcapsules with the outermost layer of PAH were prepared by removal of silica cores with hydrofluoric acid (HF). Third, chromatophore vesicles were coincubated with monodispersed $(PSS/PAH)_5$ capsules at pH 6.5 so that the vesicles were fused on the surface of the microcapsules by electrostatic interaction and osmotic pressure to obtain the RBMS colloidal motors. Scanning electron microscopy (SEM) and dynamic light scattering (DLS) were performed to characterize the cultured *R. sphaeroides*. Figure S1 shows that mature bacteria were approximately spherical and had a tightly distributed average diameter of 1 μm, in agreement with the literature report (*31*). The confocal laser scanning microscopy (CLSM) image in Fig. 2A displays that the as-separated chromatophore vesicles with strong green fluorescence at an excitation wavelength of 488 nm were monodispersed. The inset transmission electron microscopy (TEM) image in Fig. 2A exhibits a closed and collapsed structure of the chromatophore vesicle. The atomic force microscopy (AFM) image (Fig. 2B) shows that the thickness of the dried chromatophore vesicle was about 10 nm, corresponding to a lipid bilayer thickness of around 5 nm. The hydrodynamic diameter of the chromatophore vesicles was about 110 ± 2.02 nm according to the DLS measurement (Fig. 2C). These results demonstrate the successful separation of the chromatophore vesicles with an average diameter of 100 nm.

In addition, the SEM images of the dried $(PSS/PAH)_5$ microcapsules exhibit a well-defined hollow and folded structures (fig. S2A). By adding 1% rhodamine-labeled PAH as assembling components, the red fluorescence circles appear on the shell of the microcapsules in water when excited at 532 nm, implying the structural integrity of the hollow microcapsules (fig. S2B). The ultraviolet (UV)–visible (vis)–near infrared (NIR) absorption spectra (Fig. 2D) reveal that the chromatophore vesicles exhibited seven characteristic absorption peaks at 375, 447, 475, 508, 590, 800, and 850 nm ranging from the UV to NIR regions due to the presence of bacteriochlorophylls and carotenoid pigments (*32*). In addition, the surface potential analysis was conducted to monitor the assembly process of RBMS colloidal motors (Fig. 2E). The initial surface potential of the chromatophore vesicles and the as-assembled $(PSS/PAH)_5$ capsules with the outermost layer of a positively charged PAH were −35.2 and +8.12 mV, respectively. After fusion of the chromatophore vesicles on the $(PSS/PAH)_5$ capsules, the surface potential of as-prepared RBMS motors was changed to −29.9 mV. The SEM images of the dried RBMS colloidal motors in Fig. 2F had a similar hollow and folded structure with the dried $(PSS/PAH)_5$ microcapsules. Furthermore, the AFM images of the dried RBMS motors (Fig. 2G) and $(PSS/PAH)_5$ capsules (fig. S2C) show that the surface roughness of RBMS motors became higher after the fusion of the chromatophore vesicles. Accordingly, the wall thickness of the dried RBMS motors increased to ~5 nm compared to $(PSS/PAH)_5$ capsules, corresponding to a lipid bilayer thickness of the chromatophore vesicles (*33*). From the selected square area in Fig. 2G, the enlarged AFM image at the upper shows a protrusion of the chromatophore lipid surface on the RBMS motor (Fig. 2H). The height is about 11 nm higher than the protein-enriched lipid membrane, corresponding to the height value of F_OF_1-ATPase protruded from the lipid layer (*34*). In addition, this result is also similar to the previous AFM measurements of F_OF_1-ATPase in native chromatophore vesicles (*35*). It thus provides a direct observation that F_OF_1-ATPase has been successfully assembled onto the RBMS motor. Given the intrinsic characteristic absorption of the assembled chromatophore membranes, the CLSM image shows the continuous green fluorescence over the RBMS motors at an excitation wavelength of 488 nm (*36*). Moreover, the fluorescence intensity of the shell of the RBMS colloid motors was

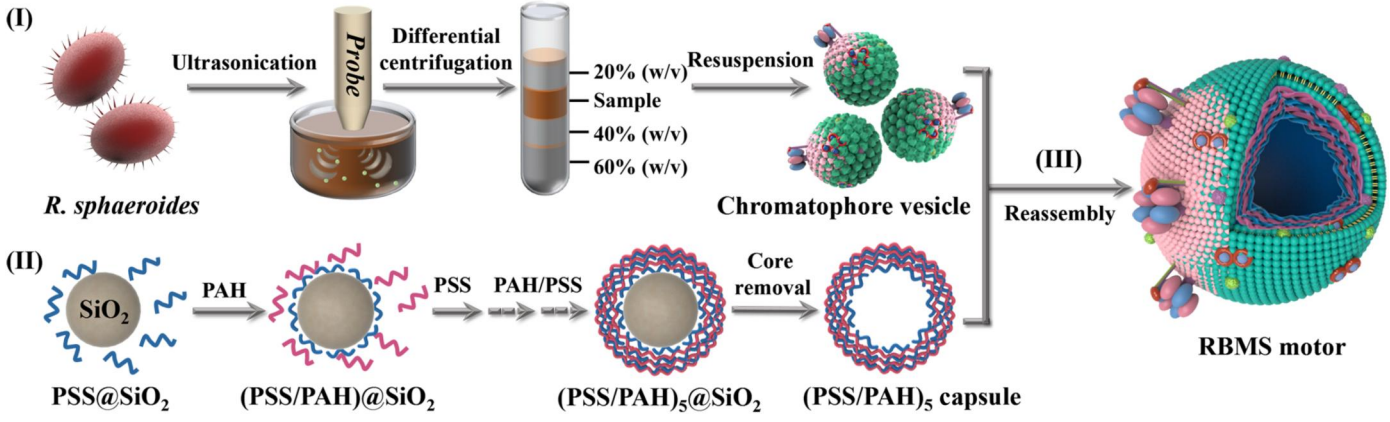

Fig. 1. Schematic illustration of the hierarchical assembly of RBMS colloidal motors. (**I**) Isolation of chromatophore vesicles from *R. sphaeroides*. (**II**) Preparation of $(PSS/PAH)_5$ microcapsules via a template-assisted layer-by-layer self-assembly strategy. (**III**) The RBMS colloidal motor was obtained by fusion of chromatophore vesicles on the $(PSS/PAH)_5$ microcapsules.

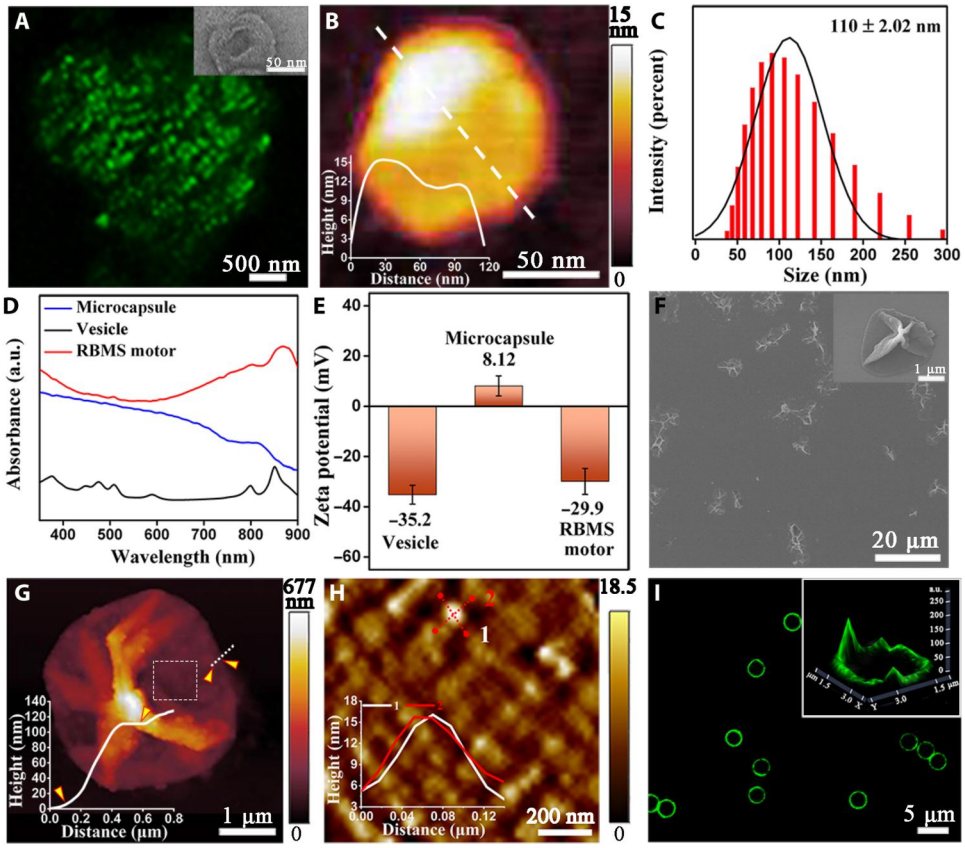

Fig. 2. The characterization of RBMS colloidal motors. (**A** and **B**) CLSM and AFM images of an isolated chromatophore vesicle. The inset is a TEM image of vesicles. (**C**) Size distribution of the chromatophore vesicles. (**D**) UV-vis-NIR absorption spectra of chromatophore vesicles, $(PSS/PAH)_5$ capsules, and RBMS motors. (**E**) Zeta potential of different samples. (**F**) SEM image of RBMS motors in a dried state. The inset is an enlarged image. (**G**) AFM image of an RBMS colloidal motor and the corresponding height profile for an indicated area. (**H**) Enlarged AFM image of the selected square area in (G) with F_OF_1-ATPase in the top panel. Inset: Two profiles showing the height of F_OF_1-ATPase, 11.2 ± 0.15 nm and 11.8 ± 0.12 nm. (**I**) CLSM image of RBMS motors at an excitation wavelength of 488 nm. The inset is a corresponding 3D CLSM image of florescence intensity of an RBMS colloidal motor.

inhomogeneously distributed as shown in Fig. 2I, which was further confirmed by the corresponding three-dimensional (3D) CLSM image of florescence intensity in the inset, representing the asymmetric distribution of chromatophore proteins and F_OF_1-ATPase molecular motors on the surface membrane of the RBMS motors. In this case, one side of our RBMS motor enriched F_OF_1-ATPase protein motors, which may be regarded as a classical Janus colloidal motor. Together, the RBMS colloidal motors with an asymmetrical distribution of F_OF_1-ATPase protein molecular motors and chromatophores were successfully obtained.

Given that the F_1 parts of rotary F_OF_1-ATPase protein molecular motors in the natural chromatophore vesicles extend outward, the orientation of F_OF_1-ATPases in the as-assembled RBMS colloidal motors is critically important for their self-propulsion. Our previous studies have demonstrated that the spreading process of liposomes on the surface of soft polyelectrolyte multilayers with the top surface of a positively charged polyelectrolyte follows a "parachute" fusion mechanism as illustrated in fig. S3 (*37*, *38*). Upon chromatophore vesicles spreading on the $(PSS/PAH)_5$ microcapsule with the outermost layer of PAH according to this parachute model, it results in well-defined lipid bilayers with both the outside-up and inside-up oriented F_OF_1-ATPases. The ratio between inner and outer leaflets of lipid bilayers could be calculated by $\tan^2(\theta/2)$, where θ is the contact angle between the surface of the vesicle and that of the microcapsule. The contact angle was estimated to be about 50°, indicating the formation of lipid bilayer with about 40% inner leaflet and 60% outer leaflet in the original segments facing upward orientation (*38*). According to the surface area ratio between a vesicle and a microcapsule, it was calculated to be ~900 vesicles with a diameter of 110 nm for the full coverage of lipid bilayers on each $(PSS/PAH)_5$ microcapsule with an average diameter of 3 μm. Because of approximately one F_OF_1-ATPase protein per chromatophore vesicle (*31*), it is supposed that three-fifths of the assembled F_OF_1-ATPases (i.e., 540) should orientate outward.

Motion and analysis of RBMS motors

To propel the RBMS colloidal motors with the asymmetric distribution of F_OF_1-ATPases, light illumination was used to trigger the generation of proton gradients and then the ATP synthesis was catalyzed by the assembled F_OF_1-ATPases as schematically illustrated in Fig. 3A. Note that four different excitation wavelengths (365, 488, 543, and 850 nm) were selected due to the wide characteristic absorption of chromatophores ranging from UV to NIR regions. The typical trajectories of RBMS motors are shown in Fig. 3B,

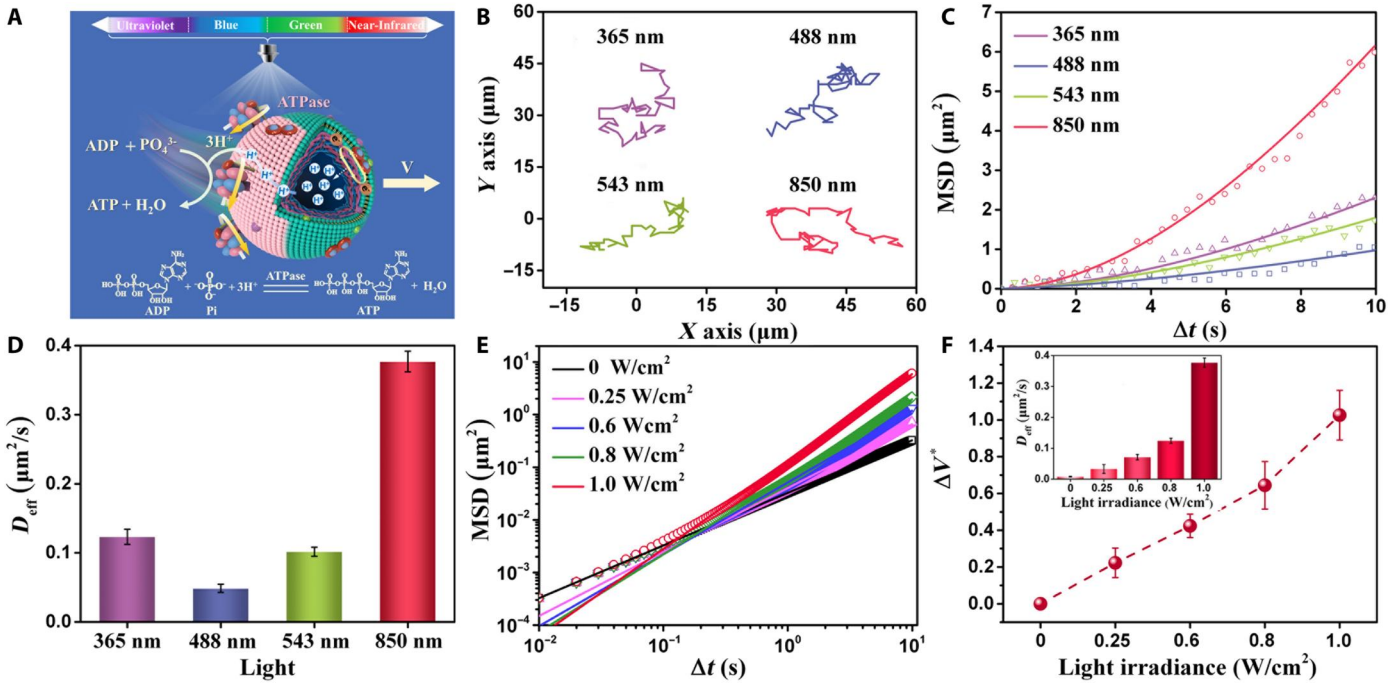

Fig. 3. Autonomous motion behavior of the RBMS motor. (**A**) Schematic illustration of the motion of an RBMS colloidal motor. Under light illumination, a transmembrane proton gradient is generated to drive ATPase molecular motors to synthesize ATP from ADP and Pi. (**B**) Movement trajectories of RBMS colloidal motors under 1 W/cm^2 at different wavelengths of light over 10 s. (**C** and **D**) MSD versus time interval and diffusion coefficient of RBMS colloidal motors at 1 W/cm^2 of the UV light (△), blue light (□), green light (▽), and NIR light (○) over 9 s. (**E**) MSD versus time interval of the RBMS colloidal motors at different NIR light irradiances over 9 s. Here, the relevant diffusion exponents are 1.00 (0 W/cm^2, □), 1.21 (0.25 W/cm^2, ◇), 1.36 (0.6 W/cm^2, △), 1.47 (0.8 W/cm^2, ▽), and 1.66 (1.0 W/cm^2, ○), respectively. (**F**) Relative speed increment and the diffusion coefficient (inset) of RBMS colloidal motors at different NIR light irradiances over 9 s.

captured from movie S1, under light irradiation at a power of 1 W/cm^2 over 10 s. Given that the refractive index of two faces of the RBMS motors is almost identical, it is difficult to distinguish between active face and passive face under an optical microscope like those metal-coated Janus motors. To verify the direction of motion, an Au-coated Janus RBMS motor with a diameter of 3 μm was used as illustrated in fig. S4. Here, the Au side served as the passive face, and the chromatophore vesicles were assembled onto the other side as the active face. It can be found that the direction of motion of Janus RBMS motors is opposite to the active face. Hence, by analogy with that of Au-coated Janus RBMS motors, it is supposed that our RBMS motors moved along the direction from the active face to the passive face.

Different trajectory lengths of the RBMS motors reflect their propulsion abilities under various lights. Then, the mean square displacement (MSD) versus time was used to study the enhanced motion of RBMS motors governed by the equation

$$\mathrm{MSD} = 4D\Delta t + \frac{V^2\tau_R{}^2}{2}\left[\frac{2\Delta t}{\tau_R} + e^{-\frac{2\Delta t}{\tau_R}} - 1\right] \propto \Delta t^{\alpha}$$

with the diffusion coefficient D, the time interval Δt, the rotational time τ_R, the RBMS motor's propulsion speed V, and the anomalous diffusion exponent α (*39*, *40*). The MSD curves in Fig. 3C display light irradiance–dependent anomalous diffusion, whose diffusion exponents are 1.48 (365 nm), 1.29 (488 nm), 1.43 (543 nm), and 1.66 (850 nm), respectively (fig. S5A). It exhibits the environment-dependent motion abilities of RBMS colloidal motors. Similarly, Fig. 3D shows the highest effective diffusion coefficient D_{eff} (corresponding to $D_{\mathrm{eff}} = D + \frac{1}{4}V^2\tau_R$) of the RBMS motors under illumination of 850 nm, corresponding to the fastest speed of about 1.41 μm/s (fig. S5B). We further considered the influence of light irradiance at 850 nm on the motion of the RBMS motors. The trajectories (fig. S6A, taken from movie S2) and the corresponding MSD versus time interval (fig. S6B) of the RBMS motors suggest the increasing motion ability with the enhanced intensity of 850-nm light irradiance. Particularly, the relevant diffusion exponents in Fig. 3E were 1.00 (0 W/cm^2), 1.21 (0.25 W/cm^2), 1.36 (0.6 W/cm^2), 1.47 (0.8 W/cm^2), and 1.66 (1.0 W/cm^2), respectively, suggesting a light irradiance–dependent nonlinear behavior from Brownian diffusion to active enhanced diffusion. To quantitatively characterize the speed increment with the intensity of light irradiance, a dimensionless relative speed increment ΔV^* is defined as $\Delta V^* = (\overline{V}_p - \overline{V}_B)/\overline{V}_B$, where $\overline{V}_p$ is the self-propelled speed of an RBMS motor and $\overline{V}_B$ is its Brownian motion speed. ΔV^* as a function of light irradiance was plotted, where ΔV^* increased up to 1.02 at 1 W/cm^2 of light irradiance and the corresponding effective diffusion coefficient was 0.38 μm/s^2 (the inset in Fig. 3F). These results display that the increasing intensity of light irradiance could efficiently enhance the directional propulsion of RBMS motors. Totally, the RBMS colloidal motors with an asymmetric distribution of F_OF_1-ATPases and chromatophore proteins could autonomously move under light illumination with different wavelengths ranging from UV to NIR. The RBMS motors exhibit the highest speed under exposure of 850-nm NIR light, and their speed may be regulated by changing the intensity of light irradiance.

It is worth noting that in our case, the effect of the hydrodynamic flow became unimportant because the Reynolds number *Re* is about 10^{-3}. Golestanian *et al.* (*41*) theoretically predicted that the molecular machines should produce a diffusiophoretic force equivalent of the jet engine by releasing asymmetrically the reaction products in fluids, instead of acquiring an inertial force by expelling the exhaust.

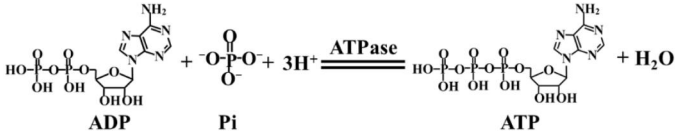

ATP biosynthetic of RBMS motors

To gain further molecular origin of the light-activated propulsion mechanism, the photochemical reaction occurring on the surface of the RBMS colloidal motors was first examined. As mentioned above, the chromatophore membranes on the topmost of the RBMS motors contained various light-harvesting protein complexes (e.g., LH 2 and LH 1). As illustrated in Fig. 4A, the excitation energy under light illumination was transferred to the reaction center (RC) to reduce quinone (Q) to hydroquinone (QH_2) by light-induced charge separation across the membranes. Then, electrons were shuttled back by the cytochrome cy^{2+} from the cytochrome bc1 to the RC, accompanied by the proton transfer. The transmembrane proton gradient was thus generated, and then the proton flows drove the synthesis of ATP by the embedded F_OF_1-ATPases in the presence ADP and PO_4^{3-} (*42*). Considering the exact value of the stoichiometric numbers for ADP, Pi, and ATP, the chemical equation is proposed as follows (*34*). It is worthy to note that the synthesis of one ATP molecule catalyzed by F_OF_1-ATPases still requires three protons besides ADP and Pi as indicated in the chemical equation.

The photocurrent detection was also conducted to explore the occurrence of the photochemical reaction on the RBMS motors as shown in Fig. 4B. By comparison to the bare microcapsules, the photocurrent of both the chromatophore vesicles and RBMS motors could be observed under light illumination. The photocurrent sign repeatedly appeared when light was turned on or off, suggesting that the photo-induced electron activity of the RBMS motors fully comes from the embedded chromatophore proteins. In addition, the ATP content during the photocatalytic process was quantified using high-performance liquid chromatography (HPLC). As shown in Fig. 4C, ATP was produced under light illumination with four wavelengths (365, 488, 543, and 850 nm) and the maximum ATP content was 1.82 μM under 850-nm light exposure for 5 min. The highest ATP production rate was 0.36 μM min^{-1}, in agreement with the fastest speed under 850-nm light as mentioned above. Next, the dependence of F_OF_1-ATPase–catalyzed ATP production on the input power of 850-nm light was investigated.

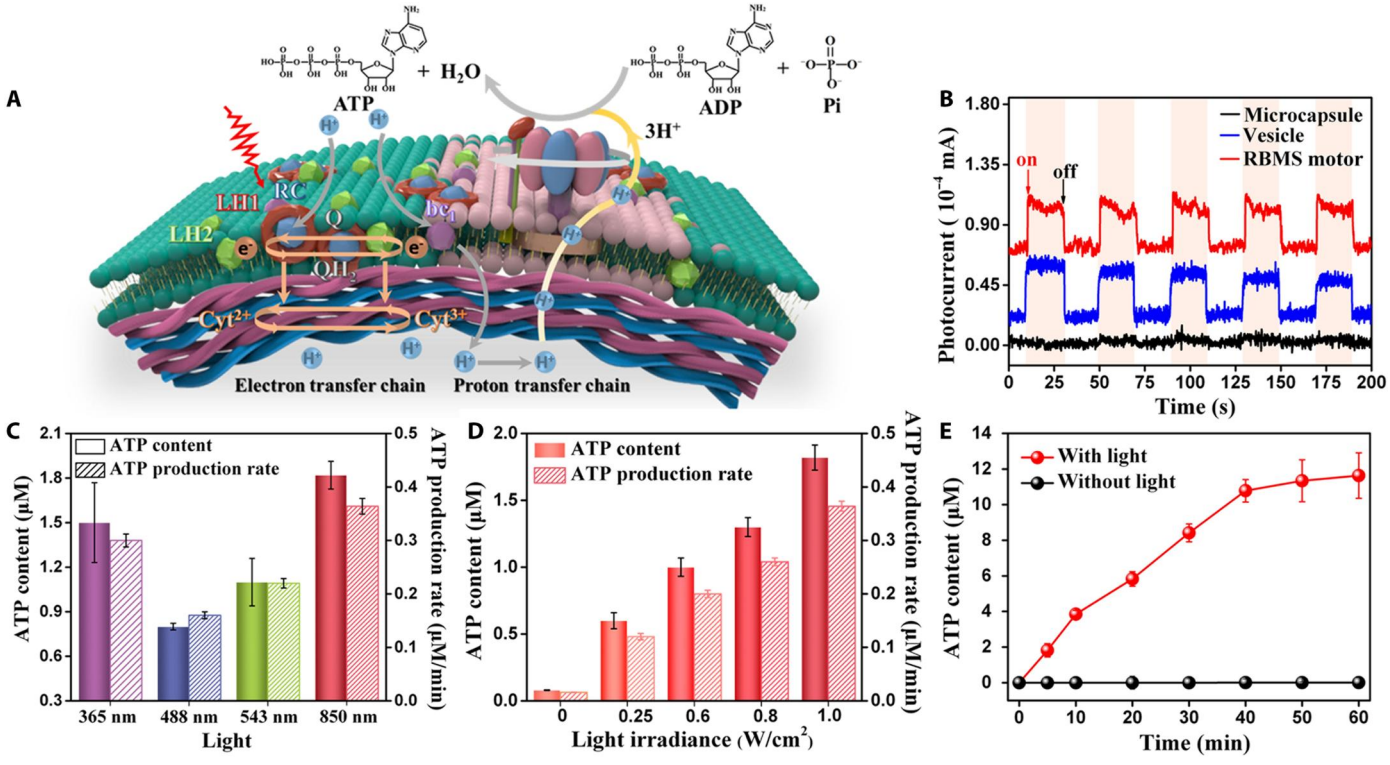

Fig. 4. Photosynthetic activity of RBMS motors. (**A**) Schematic representation of the photophosphorylation process for RBMS colloidal motors. In the presence of light, a photoinduced cyclic electron transport accompanied by transmembrane proton translocation is established and then ATPase converts ADP into ATP via phosphorylation. (**B**) Photocurrent-time curve of microcapsule, vesicle, and RBMS motor with cyclic "on" and "off" xenon lamp light. (**C**) Average ATP production and relevant production rate of the RBMS motors under 1 W/cm^2 UV, blue, green, and NIR light for 5 min. (**D**) NIR light intensity–dependent ATP synthesis and ATP-producing rate by RBMS colloidal motors for 5 min of illumination. (**E**) ATP synthesis catalyzed by RBMS colloidal motors as a function of the reaction time under 1 W/cm^2 NIR light and a control experiment in the dark.

Figure 4D shows the rapid increase of ATP content with the enhanced light intensity. Particularly, the ATP production of the RBMS motors was 1.82 μM at 1.0 W/cm^2, whereas the ATP content at 0 W/cm^2 was about 0.08 μM, approaching zero. In addition, the ATP production gradually increased with the illumination time in 40 min and then slowly went up (Fig. 4E). The corresponding ATP production rate slowed down with the elongated illumination time after 5 min due to the product inhibition and a loss of photosynthetic activity (fig. S7). Given that the transmembrane proton gradient determined the ATP production rate, we measured the time-dependent internal pH changes. With the illumination time increasing, the fluorescence intensity at 405 and 453 nm changed gradually, whereas the fluorescence intensity remained almost constant without light irradiation (fig. S8, A and B). The calculated pH values decreased rapidly in 20 min, following a slow reduction. By comparison, the pH values were barely unchanged in the absence of light (fig. S8C). This result is in good agreement with the change of ATP production rate, suggesting the ATP biosynthesis driven by the continuous transmembrane proton flow. Furthermore, the typical ATP production rate is up to ~100 ATP s^{-1} per F_OF_1-ATPase from the chromatophore vesicles according to a previous report (*31*). In this case, the number of the outward-orientated F_OF_1-ATPases was calculated to be about 1.1×10^{10} in the detection volume of 300 μl. Considering that the loss amount during the assembly process was about 20%, the number of as-prepared $(PSS/PAH)_5$ microcapsules was about 6×10^7 (the concentration of SiO_2 templates was 50 mg/ml, and the detection volume was 50 μl). Consequently, about 183 of F_OF_1-ATPases with outward orientation were assembled on each $(PSS/PAH)_5$ microcapsule, which could collectively propel the RBMS colloidal motors. Note that the experimental value was smaller than the theoretical maximum value because the chromatophore membranes spreading on the $(PSS/PAH)_5$ microcapsules were not highly condensed and the distribution of F_OF_1-ATPases was random. Overall, these results demonstrate the occurrence of the photophosphorylation process on the surface of the RBMS colloidal motors and the subsequent ATP production upon light irradiation. The transmembrane protons could be fully used for the F_OF_1-ATPase–catalyzed synthesis of ATP from ADP, Pi, and H^+. Hence, the resulting proton concentration gradient around F_OF_1-ATPases could be neglected, and thus, the contribution of proton concentration gradient on the self-propulsion of RBMS motors was excluded.

Propulsive mechanism of RBMS motors

On the other hand, the substrate Pi has little effect on the photophosphorylation process unless at a high concentration (*43*), so only the influence of various ADP concentrations on the self-propulsion of RBMS motors under 850-nm light irradiance at 1 W/cm^2 was considered. The MSD versus time intervals of the RBMS motors in Fig. 5A show an ADP concentration–dependent nonlinear diffusion behavior, whose diffusion exponents are 1.00 (0 mM ADP), 1.25 (0.1 mM ADP), 1.52 (0.5 mM ADP), 1.66 (1.0 mM ADP), and 1.59 (5.0 mM ADP), respectively (fig. S9A). Figure 5B displays that the effective diffusion coefficient D_{eff} gradually improved with the increasing ADP concentrations and reached a maximum value of 0.39 μm^2/s in 1 mM ADP. Similarly, the self-propelled speed of the RBMS motors was enhanced from 0.73 μm/s at 0 mM ADP to 1.41 μm/s in 1 mM ADP, but decreased to 1.21 μm/s in 5 mM ADP. Accordingly, the ATP production rate of the RBMS motors in 1 mM ADP was higher than those under other concentrations, indicating that the ATP synthesis reached a saturated state (fig. S9B). In contrast, the excess of ADP substrates inhibited the enzymatic activity of F_OF_1-ATPases (*43*), thus slowing down the active diffusion of the RBMS motors above 1 mM ADP. Furthermore, we examined the self-propulsion of the RBMS motors with or without the assembled chromatophore vesicles, ADP, Mg^{2+}, and PO_4^{3-} under 850-nm illumination at 1 W/cm^2. As shown in Fig. 5C, the MSD curves of the RBMS motors indicate that the RBMS motors exhibited different diffusion behaviors under different reaction conditions. The diffusion exponents of RBMS motors in the absence of chromatophore, ADP, Mg^{2+}, PO_4^{3-}, and the complete reaction conditions were 1.00, 1.11, 1.33, 1.09, and 1.66, respectively (fig. S10A). The effective diffusion coefficient and speed of RBMS motors in the incomplete reaction systems were much smaller than those of intact RBMS motor system, as shown in Fig. 5D. In addition, we found that the ATP biosynthesis is strongly dependent on F_OF_1-ATPase, light-induced proton gradient, substrate ADP and PO_4^{3-}, as well as Mg^{2+} for activating enzymes (fig. S10B). All of these results demonstrate that the motion of RBMS motors mainly originates from the local concentration gradient of reactants and products caused by ATP biosynthesis, whereas the transported protons across the membrane are almost consumed in the ATP synthesis, and thus, a direct contribution of proton concentration gradient on the motion could be neglected. Moreover, the numerical simulation result indicates that the local concentration gradient of the reactant ADP is formed in the vicinity of the RBMS motor induced by the asymmetric ATP synthesis reaction (Fig. 5E). Last, both the rate of ATP production and the speed of the RBMS motor synchronously increase with the enhancing light irradiance as shown in Fig. 5F. Given the maximum number of ATP formation by F_OF_1-ATPase, under illumination of 0.25, 0.6, 0.8, and 1.0 W/cm^2, the working F_OF_1-ATPase protein motors on the surface of an RBMS colloidal motor are estimated to be at least 8, 60, 100, 130, and 183, respectively. As the light intensity increases, so does the rate of proton generation, resulting in a large enough proton motive force to drive more ATPase rotation (*44*). Note that the proton motive force across the membrane drives the central stalk, which connects F_O and F_1, rotating at a rate of 20 Hz (*45*). The rotation of the central stalk results in the conformational change of F_1 part to synthesize ATP from ADP, PO_4^{3-}, and H^+. Obviously, the rotation of the central stalk in the F_OF_1-ATPase protein motor generates a local fluid flow around F_OF_1-ATPase and thus enhances the chemical diffusion. Because each RBMS motor roughly contains 183 F_OF_1-ATPases, they can further accelerate the diffusion of chemicals through their collective rotation, thus increasing the intensity of the local concentration gradients. In other words, the motion of an RBMS colloidal motor is collectively powered by F_OF_1-ATPases involved in the photophosphorylation. Together, our findings indicate that the concentration gradient of the reactants ADP and PO_4^{3-} generated by the collective rotation of F_OF_1-ATPase biomolecular motors consuming ADP and PO_4^{3-} to synthesize ATP results in a self-diffusiophoretic force to propel the RBMS motors.

DISCUSSION

We have successfully demonstrated a type of cell-mimic F_OF_1-ATPase–powered supramolecular Janus colloidal motors and studied the ATP biosynthesis–dependent self-propulsion by the

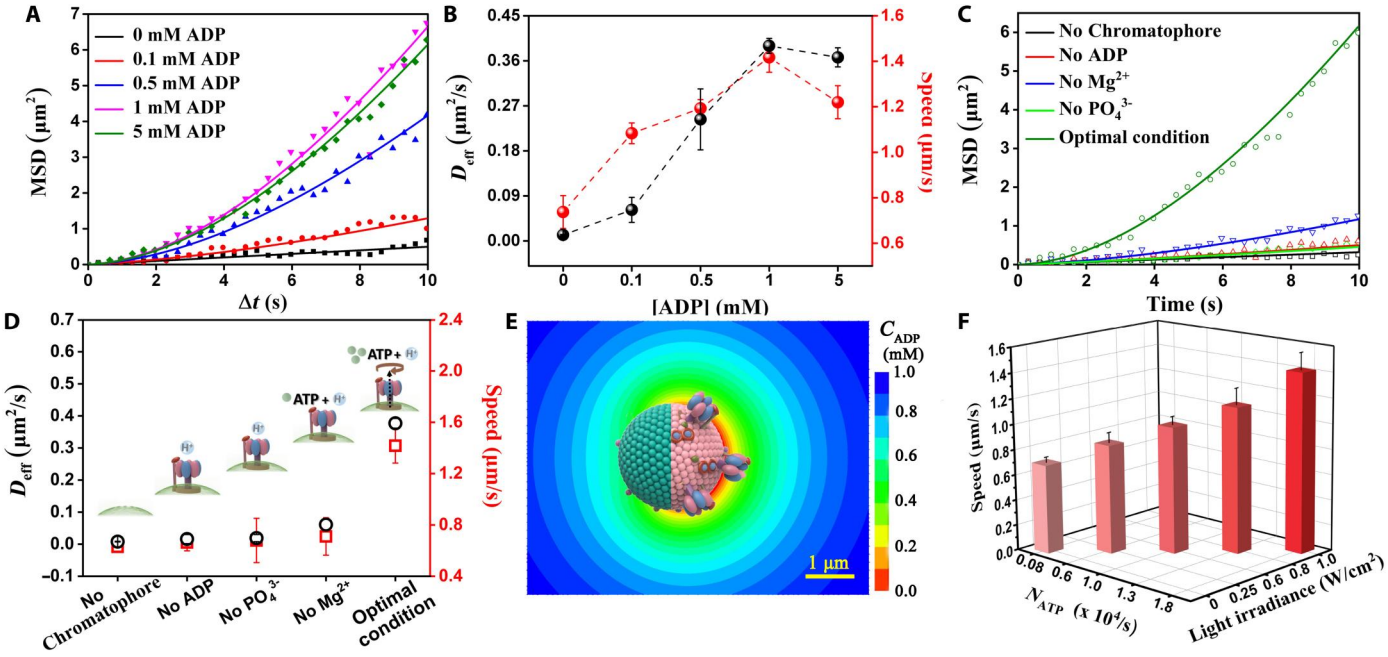

Fig. 5. Motion analysis of RBMS motors under different concentrations of substrate and reaction conditions. (**A**) MSD versus time interval of RBMS colloidal motors in various concentrations of ADP solution under 1 W/cm^2 light at 850 nm for 5 min (■, 0 mM ADP; ●, 0.1 mM ADP; ▲, 0.5 mM ADP; ▼, 1 mM ADP; ◆, 5 mM ADP). (**B**) Diffusion coefficient (black) and speed (red) of RBMS motors in different concentrations of ADP. (**C**) MSD versus time interval of RBMS colloidal motors in no chromatophore (□), no ADP (△), no Mg^{2+} (▽), no PO_4^{3-} (◇), and an intact RBMS motor system (○) with 1 W/cm^2 light at 850 nm for 5 min. (**D**) Diffusion coefficient (black) and speed (red) of RBMS colloidal motors in various conditions. Inset: Schematic illustration of the corresponding products at different conditions. (**E**) Computer simulation of the local concentration gradient field of the reactant ADP across an RBMS motor induced by the photosynthetic phosphorylation. (**F**) The speed of the RBMS colloidal motor and the rate of ATP formation are dependent on the intensity of light irradiance used. N_{ATP} represents the number of ATP production per second for each RBMS motor.

collective rotation of as-assembled F_OF_1-ATPases under light irradiations. The Janus structure of the RBMS motors was formed by the fusion of chromatophore vesicles on the $(PSS/PAH)_5$ microcapsules through a parachute mechanism, which can control about 60% of the assembled F_OF_1-ATPases orientating outward. The average number of the outward-oriented F_OF_1-ATPases on each RBMS motor was calculated on the basis of the content and production rate of ATP determined by HPLC. The F_OF_1-ATPase motor proteins asymmetrically assembled on the microcapsules efficiently convert natural energy stored in the environments into chemical energy ATP by metabolic reactions and create a local chemical gradient providing the diffusiophoretic force to propel the colloidal motors. Because of the wavelength-dependent catalytic activity of the chromatophore vesicles, the ATP production rate of RBMS motors could be regulated not only by changing the chemical reaction conditions but also by modulating the external light. Moreover, because of their adaptability to environments, the speed of the RBMS motors is highly controllable by tuning light irradiance, wavelength, and ADP concentration. The appearance of superdiffusion behaviors, whose mean free path is much longer than that of environmental thermal noise, allows effective directional motion of RBMS motors. Note that the rotation of F_OF_1-ATPases occurs in the 2D membrane plane and the size of the central stalks is so small (~1 nm) that the rotation can cause a torque but has negligible effect on the swimming motion of the RBMS colloidal motors at low Reynolds number. In contrast, bacterial motion is dependent on a rotary protein motor at its base and the protein flagella. Without long flagella, bacteria cannot swim. Theoretically, if one can attach artificial flagella onto the β or c subunits as previously reported (*46*, *47*), our RBMS colloidal motors may be directly propelled by the rotary motion of F_OF_1-ATPases, like swimming bacteria.

Our work is an innovative exploration, and the framework proposed here provides a prototypical paradigm to use natural protein motors as the power engine to drive artificial supramolecular colloidal motors and has substantially extended the application scenarios of conventional colloidal motors. Such biofunction-integrated RBMS motors hold great potential to provide not only a comprehensive construction platform for cell-like autonomous mobile microdevices but also a promising arena for precision medicine such as active targeted delivery in the future.

MATERIALS AND METHODS

Materials

Bacteria of *R. sphaeroides* was purchased from the Chia General Microbiological Culture Collection Center. The silica spheres with a diameter of 3 μm were obtained from Baseline Chromtech Research Center, Tianjin, China. PAH [weight-average molecular weight (M_w) = 50,000], PSS (M_w = 70,000), tetramethylrhodamine isothiocyanate, and deoxyribonuclease (DNase) were purchased from Sigma-Aldrich. Tris-HCl (0.5 M, pH 8.0) was obtained from Biotopped, China. Magnesium chloride ($MgCl_2$), citrate, sodium dihydrogen phosphate (NaH_2PO_4), and magnesium sulfate ($MgSO_4$) were purchased from Sinopharm Chemical Reagent. Adenosine-

5′-triphosphoric acid disodium salt (ATP Na_2) and ADP were from Ark Pharm (America) and Klamar (China), respectively. HF was used as received without further purification. Ultrapure water with a resistivity of 18.2 megohm·cm was produced with a Purelab ultrapure water system (ElGA Purelab, UK) for all the experiments.

Culture of *R. sphaeroides*

Bacterial cells were grown in 1 liter of medium (pH 6.9 at 34°C) according to previous studies (*31*, *48*). Medium 27 should be sterilized at 121°C for 15 min before use. The cells were cultured in an artificial climate chamber (MGC-100HP-2L) under anaerobic environment and 4000 1x light. After 3 days of culture, the solution of the bacteria assumes a characteristic red brown color, and then three generations of bacteria were cultured in the medium according to the above condition.

Isolation of chromatophore vesicles

The isolated chromatophore vesicles were obtained as previously reported with modification (*48*, *49*). The photoheterotrophic culture of *R. sphaeroides* was harvested by centrifugation at 4000*g* for 10 min, and the pellet was washed twice with tris-HCl buffer (10 mM, pH 8.0) and then resuspended and homogenized in 20 ml of buffer. Few flakes of DNase and 5 mM $MgSO_4$ were added. Cells were lysed by sonication on ice (Branson Sonifier B15, 200 W, 20 min), followed by centrifugation at 6000*g* for 10 min at 4°C to obtain the supernatant. The supernatant (vesicles) was further ultracentrifuged at 140,000*g* for 120 min at 4°C, using a Beckman SW41Ti rotor. Then, the pelleted vesicles were resuspended in tris-HCl buffer and layered on a discontinuous sucrose gradient composed of 20, 40, and 60% (w/v) sucrose. After ultracentrifugation at 110,000*g*, 4°C for 4 hours, the vesicles at the interface between the 20 and 40% (w/v) sucrose layer were collected and diluted by the same volume of buffer. The obtained vesicles were further washed with buffer using ultracentrifuge at 140,000*g* for 120 min at 4°C. Finally, the vesicles were dispersed in the buffer solution. The supernatant contains chromatophore vesicles whose optical density (OD) at 850 nm is typically ~50. If needed, chromatophore vesicles can be concentrated by pelleting and resuspension.

Preparation of $(PSS/PAH)_5$ microcapsules

In a typical experiment, $(PSS/PAH)_5$ microcapsules were prepared by a template-assisted layer-by-layer assembly of polyelectrolyte layers on the surface of silica as previously described (*30*). The SiO_2 particles with a diameter of 3 μm were first suspended in PAH solution (2 mg/ml) containing 0.5 M NaCl for shaking for 15 min, followed by three repeated centrifugation/washing steps to remove the excess polyelectrolytes. Then, the silica particles were suspended in PSS solution (2 mg/ml) containing 0.5 M NaCl for 15 min under continuous shaking and washing three times using 0.5 M NaCl. The $(PSS/PAH)_5$ multilayer polyelectrolytes-adsorbed silica particles were prepared by repeating the above deposition procedure, and the outer layer was PAH. Last, the silica cores were removed by treatment with 3 M H solution. The $(PSS/PAH)_5$ microcapsules were purified by the three centrifugation/water washing steps. All obtained capsule solutions were stored at 4°C.

Fabrication of supramolecular colloidal motors

The isolated chromatophore vesicles and $(PSS/PAH)_5$ microcapsules were coincubated in the tris-HCl buffer at pH 6.5 for shaking for 30 min and kept in an ice bath. Then, the obtained colloidal motors were centrifuged and washed three times with the buffer to remove the remaining vesicles.

Characterization

SEM images were conducted with Hitachi S-5200 (Japan). TEM image was recorded by JEM 1400 (Japan), and CLSM images were taken with Zeiss LSM880 (Germany). The zeta potential and hydrodynamic diameters were measured by DLS using Malvern Zetasizer Nano S (UK). A UV-vis spectrophotometer (Shimadzu UV2600/2700) was used to characterize the UV-vis-NIR absorption peak of samples. ATP content was measured by HPLC using UltiMate E3000 (The Netherlands).

Motion measurement

The trajectories of micromotors were recorded with an Olympus BX53 fluorescence microscope (20× or 40× objective). Briefly, the RBMS colloidal motors were mixed with the reaction buffer and then dropped on a hydrophilic glass slide. The light-emitting diode (LED) light source with various wavelengths and an adjustable input power was irradiated from ~6 mm at the top of the sample. The light beam is circular with a radius of 3 mm. Optical videos were recorded with a frame rate of 30 frames per second. The trajectories of particles were analyzed by using the software ImageJ.

ATP biosynthesis

Typically, 3 ml of RBMS colloidal motors was added into 3 ml of the reaction buffer solution (pH 8.0, 20 mM tris-HCl, 10 mM NaH_2PO_4, 5 mM citrate, 10 mM $MgCl_2$, and 2 mM ADP) and mixed thoroughly. The final concentration of vesicles was at OD = 10. The light source is LED light with adjustable wavelength. A 300-μl aliquot was taken from each of the reaction systems using the HPLC method to quantify the amount of ATP.

Supplementary Materials

This PDF file includes:

Supplementary Text
Figs. S1 to S10
Legends for movies S1 and S2
References

Other Supplementary Material for this manuscript includes the following:

Movies S1 and S2

REFERENCES AND NOTES

1. Y. Jia, J. B. Li, Reconstitution of F_oF_1-ATPase-based biomimetic systems. *Nat. Rev. Chem.* **3**, 361–374 (2019).
2. S. V. Helvert, C. Storm, P. Friedl, Mechanoreciprocity in cell migration. *Nat. Cell Biol.* **20**, 8–20 (2018).
3. M. Schliwa, G. Woehlke, Molecular motors. *Nature* **422**, 759–765 (2003).
4. Y. Jia, J. Li, Molecular assembly of rotary and linear motor proteins. *Acc. Chem. Res.* **52**, 1623–1631 (2019).
5. Z. Li, X. Xu, F. Yu, J. Fei, Q. Li, M. Dong, J. Li, Oriented nanoarchitectonics of bacteriorhodopsin for enhancing ATP generation in a F_oF_1 -ATPase-based assembly system. *Angew. Chem. Int. Ed.* **61**, e202116220 (2022).

6. L. Ricotti, B. Trimmer, A. W. Feinberg, R. Raman, K. K. Parker, R. Bashir, M. Sitti, S. Martel, P. Dario, A. Menciassi, Biohybrid actuators for robotics: A review of devices actuated by living cells. *Sci. Robot.* **2**, eaaq0495 (2017).
7. X. Chen, Y. K. Xu, C. Zhou, K. Lou, Y. X. Peng, H. P. Zhang, W. Wang, Unraveling the physiochemical nature of colloidal motion waves among silver colloids. *Sci. Adv.* **8**, eabn9130 (2022).
8. R. Dong, Y. Hu, Y. Wu, W. Gao, B. Ren, Q. Wang, Y. Cai, Visible-light-driven BiOI-based Janus micromotor in pure water. *J. Am. Chem. Soc.* **139**, 1722–1725 (2017).
9. K. K. Dey, X. Zhao, B. M. Tansi, W. J. Mendez-Ortiz, U. M. Cordova-Figueroa, R. Golestanian, A. Sen, Micromotors powered by enzyme catalysis. *Nano Lett.* **15**, 8311–8315 (2015).
10. S. Tang, F. Zhang, H. Gong, F. Wei, J. Wang, Enzyme-powered Janus platelet cell robots for active and targeted drug delivery. *Sci. Robot.* **5**, eaba6137 (2020).
11. B. Wang, K. F. Chan, K. Yuan, Q. Q. Wang, X. F. Xia, L. D. Yang, L. Zhang, Endoscopy-assisted magnetic navigation of biohybrid soft microrobots with rapid endoluminal delivery and imaging. *Sci. Robot.* **6**, eabd2813 (2021).
12. Z. G. Wu, L. Li, Y. R. Yang, P. Hu, Y. Li, S.-Y. Yang, L. V. Wang, W. Gao, A microrobotic system guided by photoacoustic computed tomography for targeted navigation in intestines in vivo. *Sci. Robot.* **4**, eaax0613 (2019).
13. L. Xie, M. Yan, T. Y. Liu, K. Gong, X. Luo, B. Qiu, J. Zeng, Q. R. Liang, S. Zhou, Y. J. He, W. Zhang, Y. L. Jiang, Y. Yu, J. Y. Tang, K. Liang, D. Y. Zhao, B. Kong, Kinetics-controlled super-assembly of asymmetric porous and hollow carbon nanoparticles as light-sensitive smart nanovehicles. *J. Am. Chem. Soc.* **144**, 1634–1646 (2022).
14. Y. F. Tu, F. Peng, A. A. M. André, Y. Men, M. Srinivas, D. A. Wilson, Biodegradable hybrid stomatocyte nanomotors for drug delivery. *ACS Nano* **11**, 1957–1963 (2017).
15. H. Ceylan, I. C. Yasa, O. Yasa, A. F. Tabak, J. Giltinan, M. Sitti, 3D-printed biodegradable microswimmer for theranostic cargo delivery and release. *ACS Nano* **13**, 3353–3362 (2019).
16. Y. Wang, C. Zhou, W. Wang, D. Xu, F. Zeng, C. Zhan, J. Gu, M. Li, W. Zhao, J. Zhang, J. Guo, H. Feng, X. Ma, Photocatalytically powered matchlike nanomotor for light-guided active SERS sensing. *Angew. Chem. Int. Ed.* **57**, 13110–13113 (2018).
17. J. Parmar, D. Vilela, K. Villa, J. Wang, S. Sanchez, Micro- and Nanomotors as active environmental microcleaners and sensors. *J. Am. Chem. Soc.* **140**, 9317–9331 (2018).
18. J. Orozco, G. Cheng, D. Vilela, S. Sattayasamitsathit, J. Wang, Molecularly imprinted polymer-based catalytic micromotors for selective protein transport. *J. Am. Chem. Soc.* **135**, 5336–5339 (2013).
19. J. V. Vaghasiya, C. C. Mayorga-Martinez, S. Matejkova, M. Pumera, Pick up and dispose of pollutants from water via temperature-responsive micellar copolymers on magnetite nanorobots. *Nat. Commun.* **13**, 1026 (2022).
20. S. K. Srivastava, M. Guix, O. G. Schmidt, Wastewater mediated activation of micromotors for efficient water cleaning. *Nano Lett.* **16**, 817–821 (2016).
21. K. Yuan, B. Jurado-Sanchez, A. Escarpa, Dual-propelled lanbiotic based Janus micromotors for selective inactivation of bacterial biofilms. *Angew. Chem. Int. Ed.* **60**, 4915–4924 (2021).
22. J. Shao, S. Cao, H. Che, M. T. De Martino, H. Wu, L. Abdelmohsen, J. C. M. van Hest, Twin-engine Janus supramolecular nanomotors with counterbalanced motion. *J. Am. Chem. Soc.* **144**, 11246–11252 (2022).
23. L. K. Abdelmohsen, M. Nijemeisland, G. M. Pawar, G. Janssen, D. A. Wilson, Dynamic loading and unloading of proteins in polymeric stomatocytes: Formation of an enzyme-loaded supramolecular nanomotor. *ACS Nano* **10**, 2652–2660 (2016).
24. Y. F. Tu, F. Peng, X. F. Sui, Y. J. Men, P. B. White, J. van Hest, D. A. Wilson, Self-propelled supramolecular nanomotors with temperature-responsive speed regulation. *Nat. Chem.* **9**, 480–486 (2017).
25. H. Wang, M. Pumera, Fabrication of micro/nanoscale motors. *Chem. Rev.* **115**, 8704–8735 (2015).
26. Y. Xing, M. Zhou, T. Xu, S. Tang, Y. Fu, X. Du, L. Su, Y. Wen, X. Zhang, T. Ma, Core@satellite Janus nanomotors with pH-responsive multi-phoretic propulsion. *Angew. Chem. Int. Ed.* **59**, 14368–14372 (2020).
27. D. P. Singh, U. Choudhury, P. Fischer, A. G. Mark, Non-equilibrium assembly of light-activated colloidal mixtures. *Adv. Mater.* **29**, 1701328 (2017).
28. S. Yu, T. Li, F. Ji, S. Zhao, K. Liu, Z. Zhang, W. Zhang, Y. Mei, Trimer-like microrobots with multimodal locomotion and reconfigurable capabilities. *Mater. Today Adv.* **14**, 100231 (2022).
29. B. J. Toebes, F. Cao, D. A. Wilson, Spatial control over catalyst positioning on biodegradable polymeric nanomotors. *Nat. Commun.* **10**, 5308 (2019).
30. Y. Wu, T. Si, J. Shao, Z. Wu, Q. He, Near-infrared light-driven Janus capsule motors: Fabrication, propulsion, and simulation. *Nano Res.* **9**, 3747–3756 (2016).
31. E. Altamura, P. Albanese, R. Marotta, F. Milano, F. Mavelli, Chromatophores efficiently promote light-driven ATP synthesis and DNA transcription inside hybrid multicompartment artificial cells. *Proc. Natl. Acad. Sci. U.S.A.* **118**, e2012170118 (2021).
32. L. Limantara, R. Fujii, J. P. Zhang, T. Kakuno, Y. Koyama, Generation of triplet and cation-radical bacteriochlorophyll a in carotenoidless LH1 and LH2 antenna complexes from Rhodobacter sphaeroides. *Biochemistry* **37**, 17469–17486 (1998).
33. S. Moya, W. Richter, S. Leporatti, H. B. Umler, E. Donath, Freeze-fracture electron microscopy of lipid membranes on colloidal polyelectrolyte multilayer coated supports. *Biomacromolecules* **4**, 808–814 (2003).
34. D. Stock, A. G. W. Leslie, J. E. Walker, Molecular architecture of the rotary motor in ATP synthase. *Science* **286**, 1700–1705 (1999).
35. S. Kumar, M. L. Cartron, N. Mullin, P. Qian, G. J. Leggett, C. N. Hunter, J. K. Hobbs, Direct imaging of protein organization in an intact bacterial organelle using high-resolution atomic force microscopy. *ACS Nano* **11**, 126–133 (2017).
36. J. C. Goedheer, Energy transfer between carotenoids and bacteriochlorophyll in chromatophores of purple bacteria. *Biochim. Biophys. Acta* **35**, 1–8 (1959).
37. C. Wen, M. Wan, X. Li, Q. He, L. Gao, W. Fang, Formation mechanism and properties of polyelectrolyte multilayer-supported lipid bilayers: A coarse-grained molecular dynamics study. *ACS Omega* **2**, 910–917 (2017).
38. J. Shao, C. Wen, M. Xuan, H. Zhang, H. Qiang, Polyelectrolyte multilayer-cushioned fluid lipid bilayers: A parachute model. *Phys. Chem. Chem. Phys.* **19**, 2008–2016 (2016).
39. J. R. Howse, R. Jones, A. J. Ryan, T. Gough, R. Vafabakhsh, R. Golestanian, Self-motile colloidal particles: From directed propulsion to random walk. *Phys. Rev. Lett.* **99**, 048102 (2007).
40. R. Metzler, J. H. Jeon, A. G. Cherstvy, E. Barkai, Anomalous diffusion models and their properties: Non-stationarity, non-ergodicity, and ageing at the centenary of single particle tracking. *Phys. Chem. Chem. Phys.* **16**, 24128–24164 (2014).
41. R. Golestanian, T. B. Liverpool, A. Ajdari, Propulsion of a molecular machine by asymmetric distribution of reaction products. *Phys. Rev. Lett.* **94**, 220801 (2005).
42. E. Altamura, F. Mavelli, F. Milano, M. Trotta, Photosynthesis without the organisms: The bacterial chromatophores, in *Advances in Bionanomaterials* (Springer, 2018), pp. 165–175.
43. P. Richard, B. Pitard, J. L. Rigaud, ATP synthesis by the F_0F_1-ATPase from the thermophilic *Bacillus* PS3 co-reconstituted with bacteriorhodopsin into liposomes: Evidence for stimulation of ATP synthesis by ATP bound to a noncatalytic binding site. *J. Biol. Chem.* **270**, 21571–21578 (1995).
44. A. Singharoy, C. Maffeo, K. H. Delgado-Magnero, D. J. K. Swainsbury, M. Sener, U. Kleinekathofer, J. W. Vant, J. Nguyen, A. Hitchcock, B. Isralewitz, I. Teo, D. E. Chandler, J. E. Stone, J. C. Phillips, T. V. Pogorelov, M. I. Mallus, C. Chipot, Z. Luthey-Schulten, D. P. Tieleman, C. N. Hunter, E. Tajkhorshid, A. Aksimentiev, K. Schulten, Atoms to phenotypes: Molecular design principles of cellular energy metabolism. *Cell* **179**, 1098–1111.e23 (2019).
45. P. Dimroth, H. Wang, M. Grabe, G. Oster, Energy transduction in the sodium F-ATPase of *Propionigenium modestum*. *Proc. Natl. Acad. Sci. U.S.A.* **96**, 4924–4929 (1999).
46. Y. Sambongi, Y. Iko, M. Tanabe, H. Omote, A. Iwamoto-Kihara, I. Ueda, T. Yanagida, Y. Wada, M. Futai, Mechanical rotation of the c subunit oligomer in ATP synthase (F_0F_1): Direct observation. *Science* **286**, 1722–1724 (1999).
47. K. Nishio, A. Iwamoto-Kihara, A. Yamamoto, Y. Wada, M. Futai, Subunit rotation of ATP synthase embedded inmembranes: *a* or β subunit rotation relativeto the *c* subunit ring. *Proc. Natl. Acad. Sci. U.S.A.* **99**, 13448–13452 (2002).
48. B. A. Feniouk, D. A. Cherepanov, N. E. Voskoboynikova, A. Y. Mulkidjanian, W. Junge, Chromatophore vesicles of rhodobacter capsulatus contain on average one F_OF_1-ATP synthase each. *Biophys. J.* **82**, 1115–1122 (2002).
49. H. Kim, X. Tong, S. Choi, J. K. Lee, Characterization of ATPase activity of free and immobilized chromatophore membrane vesicles of *Rhodobacter sphaeroides*. *J. Microbiol. Biotechnol.* **27**, 2173–2179 (2017).
50. Y. Q. Xu, J. B. Fei, G. L. Li, T. T. Yuan, X. Xu, J. B. Li, Nanozyme-catalyzed cascade reactions for mitochondria-mimicking oxidative phosphorylation. *Angew. Chem. Int. Ed. Engl.* **131**, 5628–5632 (2019).
51. A. Hazard, C. Montemagno, Improved purification for thermophilic F_1F_0 ATP synthase using *n*-dodecyl β-D-maltoside. *Arch. Biochem. Biophys.* **407**, 117–124 (2002).
52. J. L. Anderson, Colloid transport by interfacial forces. *Annu. Rev. Fluid Mech.* **21**, 61–99 (1989).
53. R. Golestanian, T. B. Liverpool, A. Ajdari, Designing phoretic micro- and nano-swimmers. *New J. Phys.* **9**, 126 (2017).

Acknowledgments: We thank J. B. Li and M. C. Yang for helpful discussion. **Funding:** This work was financially supported by the National Natural Science Foundation of China (22193033 and 22172044) and the start-up grant of Wenzhou Institute, University of Chinese Academy of Sciences (WIUCASQD2021044). **Author contributions:** J.L. and Y.L. participated in experimental procedures, data collection and analysis, and manuscript writing. Y.W. and L.Y. assisted with the data analysis and analysis. H.W. performed the theoretical calculations. Q.H. participated in the study design, discussions, and manuscript writing. **Competing interests:** The authors declare that they have no competing interests. **Data and materials availability:**

All data needed to evaluate the conclusions in the paper are present in the paper and/or the Supplementary Materials.

Submitted 26 October 2022
Accepted 20 January 2023
Published 22 February 2023
10.1126/sciadv.abg3015